EUROPEAN ORGANIZATION FOR NUCLEAR RESEARCH

Performance of the EM end-cap presampler in the 1999 testbeam run

V.M.Aulchenko, D.V.Chernyak, V.F.Kazanine,
G.M.Kolachev, V.M.Malyshev, A.L.Maslennikov,
S.G.Pivovarov, G.E.Pospelov, A.I.Choucharo, R.G.Snopkov,
A.A.Talyshev, Yu.A.Tikhonov
Budker Institute of Nuclear Physics, Novosibirsk, Russia

Abstract

Two electromagnetic end-cap presampler modules were tested together with the EM end-cap calorimeter Module 0 on H6 SPS electron beam at CERN in September-October 1999. The results on energy resolution for electrons with energy in the range $20 \div 100$ GeV and various amounts of upstream dead material are presented. They are found in agreement with simulation. It is shown that using of the presampler allows one to account for the energy loss in upstream material and thus considerably recover the degradation of the energy resolution. The results of noise and crosstalk calculation and measurement in calibration as well as in data runs are also reported.

1 Introduction

The amount of material in front of the EM end-cap calorimeter (EMEC) in the transition region with the EM barrel ($1.5 \leq |\eta| \leq 1.8$) is equivalent to $3 \div 6\ X_0$ [1] which leads to significant degradation of the energy resolution. In order to recover this degradation it was decided (September 1996) to introduce a special detector unit - the end-cap presampler [2]. In December 1997 the choice was made between two options of the presampler design [3]. The flat geometry option was approved as it provides the same physics performance at lower cost as compared to the barrel-presampler-like option. The first prototype of the end-cap presampler was successfully tested together with Module 00 of the EM end-cap calorimeter during the September 1998 H6 testbeam run. It was shown [4] that the signal to noise ratio in the presampler is high enough to provide the expected recovering of the energy resolution in the presence of dead material. The detailed analysis of the presampler performance was hampered by limited statistics taken with the presampler and by problems due to dead cells in end-cap module 00. Then the presampler design was slightly changed in order to simplify the assembling procedure (see section 2). Four new modules were fabricated and two of them were tested at CERN at SPS H6 beamline in September-October 1999 together with module 0 of the EM end-cap calorimeter.

The structure of this note is as follows. The presampler design is presented in section 2. The testbeam setup and available statistics are briefly described in section 3. The response of the electronic circuit to calibration and physics signals (convertion factors DAC to ADC, ADC to GeV) and the electronics noise are calculated and compared with the results of measurement in section 4. Results of crosstalk calculation and measurement in calibration as well as in data runs are presented in section 5. The detailed description of the algorithm of the reconstruction of energy signal in the end-cap calorimeter using the presampler is given in section 6. The energy deposition in calorimeter samplings in data and in simulation is compared in section 7. The results for energy resolution and energy linearity are presented in section 8. The summary of results is given in Conclusion.

2 Presampler design

The original design of the flat option of the EM end-cap presampler was described in [3]. The outer radius of the EM end-cap presampler is 1702 mm, the inner radius is 1232 mm. The presampler is placed in a special cavern on the back side of the cryostat cold wall. The granularity of the presampler is $\Delta\eta \times \Delta\phi = 0.025 \times 2\pi/64$, i.e. the same as in middle sampling of the calorimeter in η direction and 4 times more coarse in ϕ. This corresponds to 768 readout channels (per one end-cap). Each EM end-cap presampler consists of 32 identical azimuthal sectors (modules). The isometric view of the end-cap presampler module is shown in figure 1. The principal presampler design is shown in figure 2. Two 2 mm thick active LAr layers are formed by three electrodes parallel to the front face of the EM end-cap calorimeter. The electrodes made from double sided FR4 printed circuit boards are separated by honeycomb spacers. A negative high voltage is applied to the external electrodes and the signals are read out from central electrode segmented into pads. The capacitances of readout cells decrease with η: 125 pF at $\eta = 1.5$ and 71 pF at $\eta = 1.8$. The pads are connected by pins to the 50 Ω strip readout lines printed on the top external electrode (see figures 2,3). The strip lines are connected at the outer radius of the module to the 50 Ω coaxial cables which lead the signals to the feedthroughs. At the outer and inner radius three electrodes are glued together with 2 mm thick G10 bars.

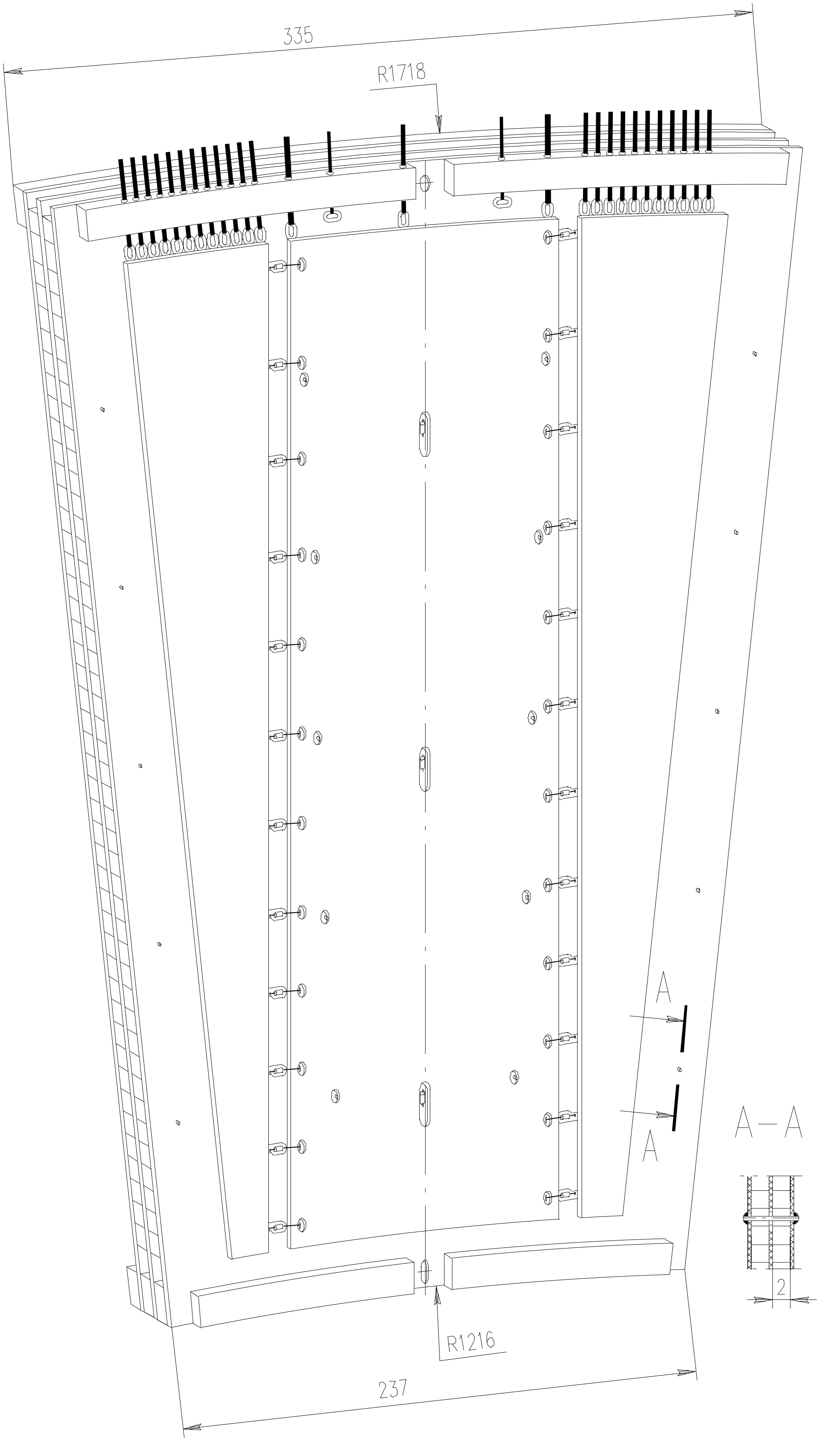

Figure 1: Isometric view of the presampler module.

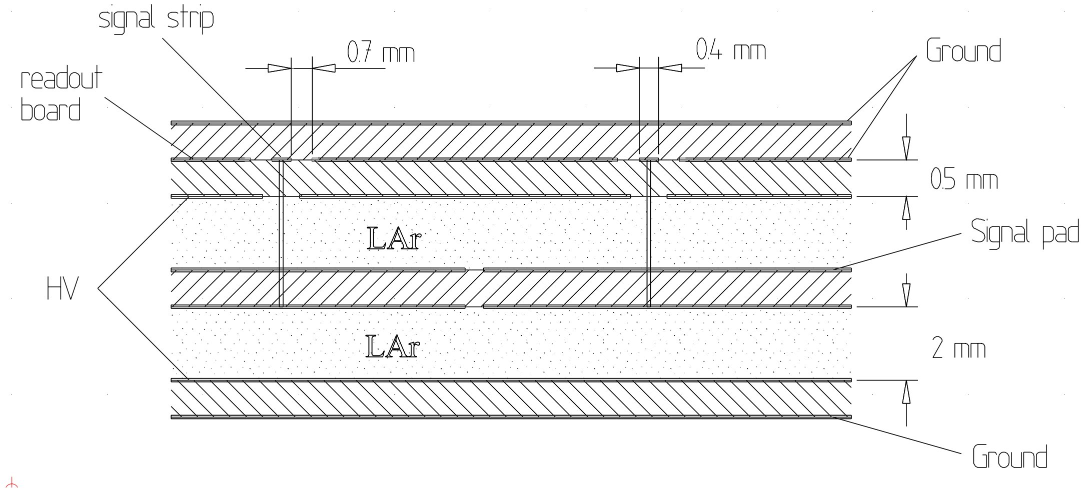

Figure 2: Principal presampler design.

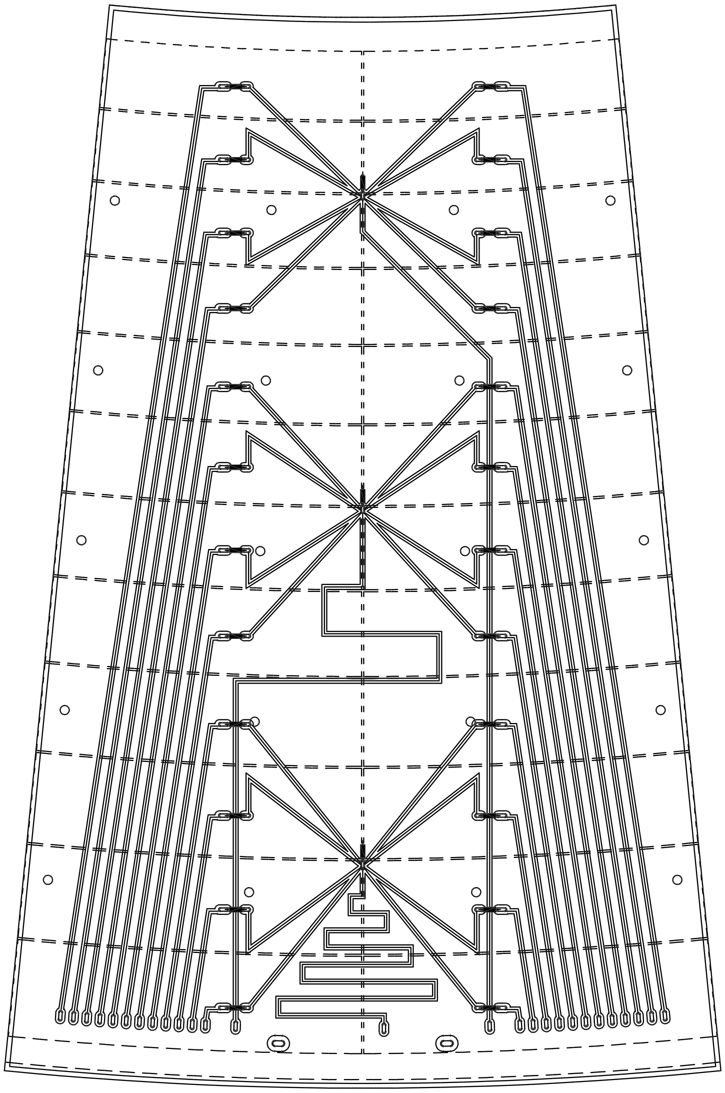

Figure 3: Strip line readout board.

3 Testbeam setup and data taken with presampler

The presampler and module 0 of the EM end-cap were placed inside the testbeam cryostat filled with liquid argon. Their relative position was very close to which will be in ATLAS. The thickness of the cryostat walls was about 0.9 X_0. The amount of upstream material before the presampler (Z=362.2 cm) was about 1.0 X_0, total amount of upstream material before the active part of the end-cap module 0 (Z=370.4 cm) was about 1.7 X_0 (see figure 4). Additional 8 mm thick iron plates could be installed or removed before the cryostat (at Z=285 cm) in order to simulate different amount of upstream dead material (up to + 3.18 X_0). The schematic view of testbeam setup is shown in figure 5.

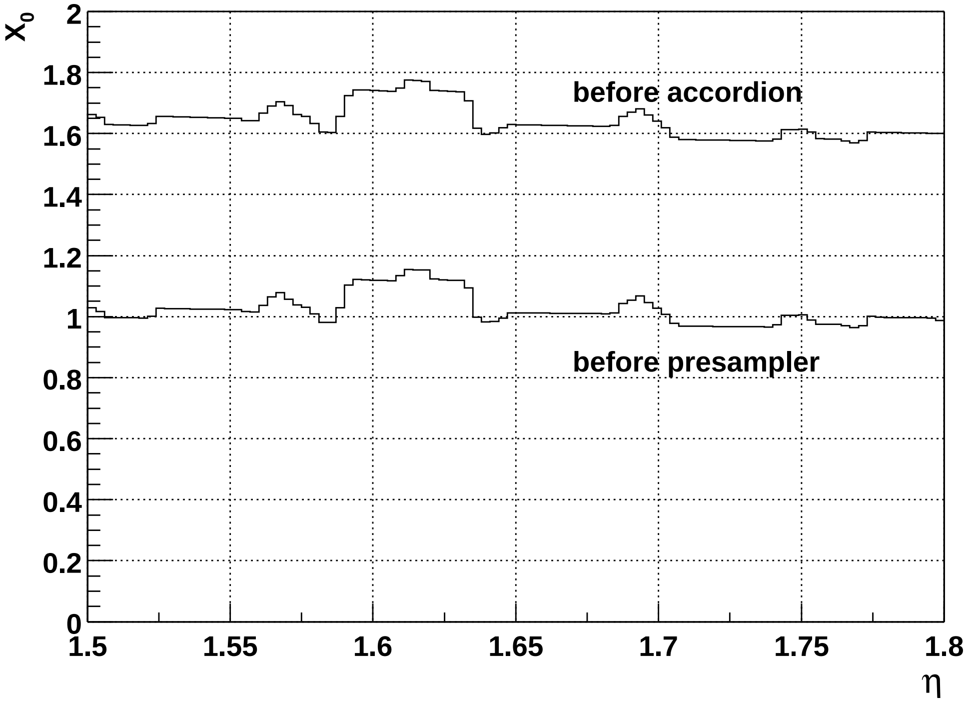

Figure 4: Amount of upstream material before presampler and accordion.

To study the presampler performance the data were taken with the SPS H6 electron beam [5] in energy region $20 \div 100$ GeV at 5 different beam positions. Figure 6 shows the points where data have been taken during presampler studies. The gray rectangle shows the area covered by two presampler modules. The most part of data was taken in point 3 (at the center of the cell in middle sampling (S2) of the EMEC, almost at the center of presampler cell) and in point $4'$ which is the intersection point of the S2 and presampler cells. The complete list of available runs taken with the presampler is given in Appendix 1.

Runs with beam energies $20 \div 100$ GeV and $1.7, 3.5, 4.4$ X_0, Point 3, were simulated in Geant 3 using the package for end-cap testbeam simulation [6]. The beam energy, η, ϕ spreads included in simulation are given in Appendix 2. The simulation was performed using the electric field map to calculate the charge collection in LAr gaps.

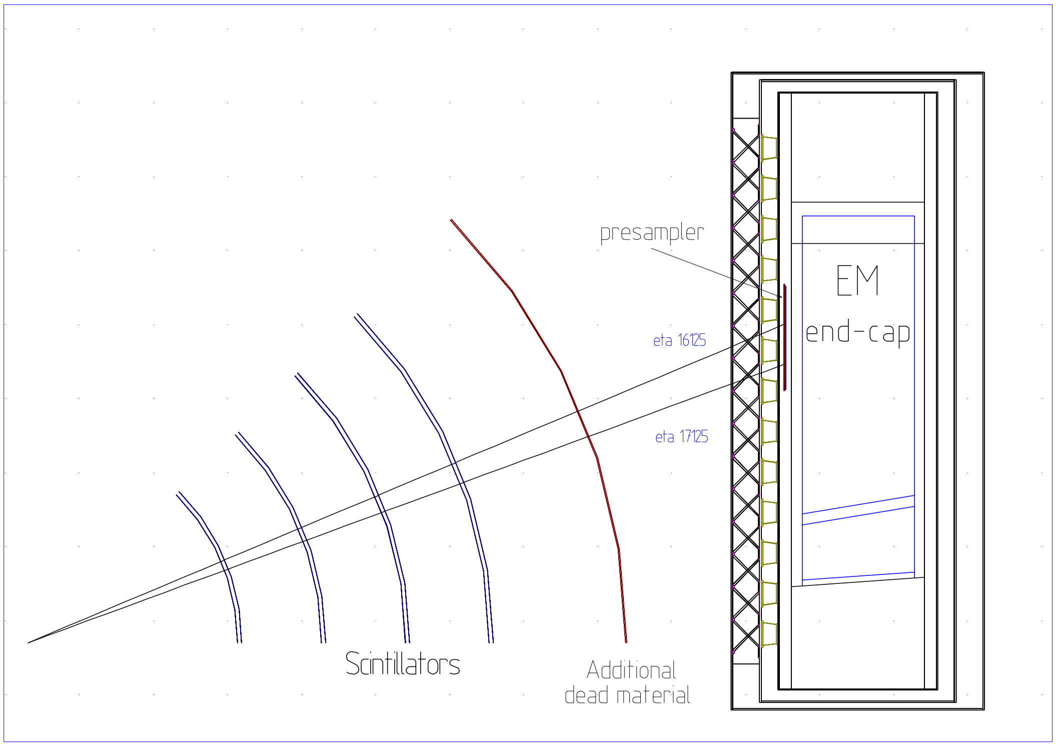

Figure 5: Schematic view of testbeam setup described in simulation. In the testbeam, the beam position was fixed while the calorimeter module position could be changed by moving the whole cryostat (η direction) or by rotating the module inside the cryostat (ϕ direction).

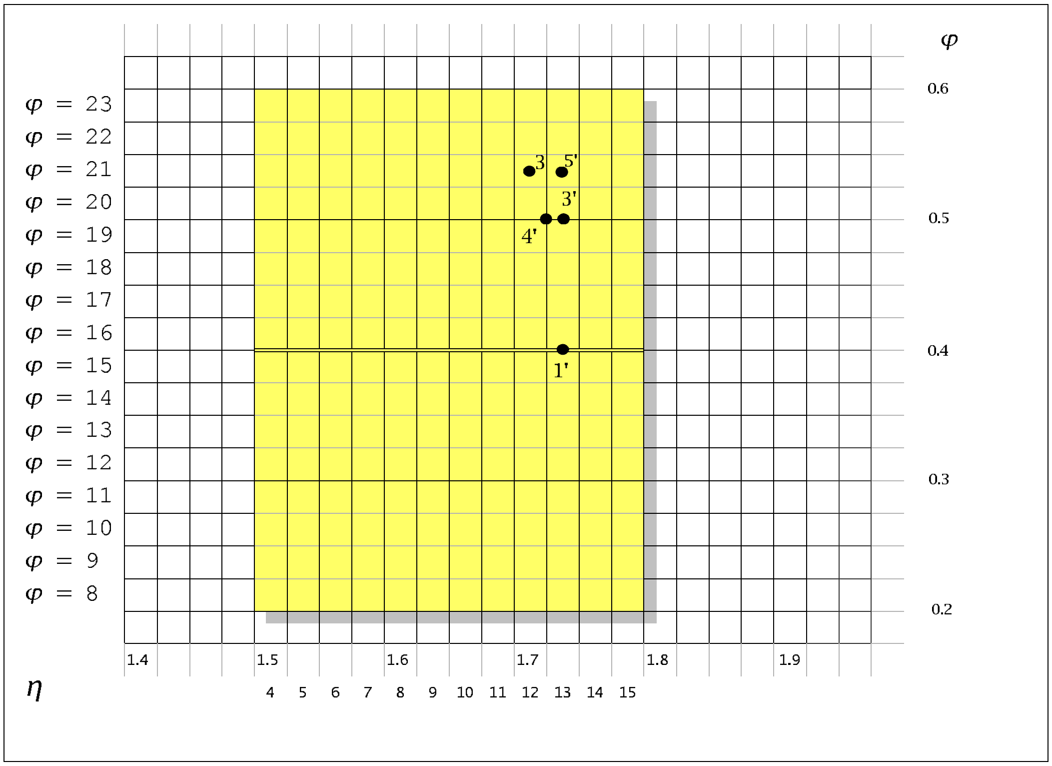

Figure 6: Map of cells in calorimeter middle section. The gray rectangle shows the area covered by two presampler modules.

4 Convertion factors DAC to ADC, ADC to GeV and noise measurement

4.1 Correspondence between DAC and ADC codes

The theoretical estimation for the correspondence between DAC and ADC codes looks like [7]

$$ADC = \frac{(2^{12}-1)\,\varepsilon\,G\,R_{ti}\,V_{DAC}^{max}}{(2^{17}-1)\,R_{eq}\,V_{ADC}^{max}}\,DAC \tag{1}$$

where $G \simeq 76$ is the shaper high gain, $R_{ti} \simeq 2.8 \cdot 10^3\,\Omega$ is the transition resistance of preamplifier, $R_{eq} = 3.48 \cdot 10^3\,\Omega$ is the calibration resistance, $V_{DAC}^{max} = 5\,$V, $V_{ADC}^{max} = 4\,$V, $\varepsilon \simeq 0.85$ is the coefficient representing the convolution with shaper transfert function. Substituting these values into the formula (1) we get the ratio ADC/DAC $\simeq 2.0$.

The measurement were performed using calibration ”delay” run. The results for 8 channel of presampler module (see figure 8) is shown in table 1.

$Channel\#$	0	1	2	3	4	5	6	7
ADC/DAC	1.783	1.846	1.838	1.829	1.828	1.835	1.856	1.866

Table 1: ADC vs DAC. Runs 103167, 103168, 103169, 103171

The average coefficient of proportionality between DAC and ADC values is equal to $\bar{A} = 1.835$, $\sigma_A = 0.025$ (1.36%). This value is used below for noise calculation. As in [7] the measured $\bar{A}$ value is 10 % lower than calculated one which could be explained by inaccurate knowledge of parameters in formula (1) and by not taking into account the SCA gain and the attenuation in cables.

4.2 Results of noise calculation and measurements

We can calculate the noise of channels from parameters of the electronics chain. The value of DAC count in units of current is

$$I_{count}^{DAC} = \frac{V_{DAC}^{max}}{(2^{17}-1)\,R_{eq}}.$$

In our case we get $I_{count}^{DAC} = 5\ V/((2^{17}-1)\cdot 3.48 \cdot 10^3\ \Omega) \sim 11$ nA. Thus, the value of one ADC count is $I_{count}^{ADC} = I_{count}^{DAC}/\bar{A} = 11/1.835 \sim 6.0$ nA. Relation between current and energy is

$$E(MeV) = I(nA)\,t_{dr}(ns)\,\frac{W_i(eV)}{1.6}\,10^{-5},$$

where $t_{dr} = 400$ ns, $W_i = 23.6$ eV [9], so $E(MeV) = 5.9 \cdot 10^{-2}\,I(nA)$. It gives the values of one DAC and ADC count in energy units of 0.65 MeV and 0.35 MeV, respectively. The preamplifier noise in our case is [8] $\sqrt{ENI^2} \sim 48$ nA (for typical detector capacitance of 100 pF, see table 2, and time of signal peaking 5 to 100 %, $t_p \sim 35$ ns) or 2.81 MeV in energy units. It corresponds to $\sigma_n \sim 8.0$ ADC counts for noise. It is worth reminding that energy deposition of MIP in two 2 mm LAr gaps equals to 0.85 MeV.

For noise estimation we used the pedestal measurements. The #103166 run was processed using standard PEDESTAL package in EMTB [10] program. The average value of incoherent noise for one presampler cell is 7.59 ADC counts, and corresponding value of coherent noise is 0.72 ADC counts. Thus the measured noise value is in good agreement with the expected one. The noise distribution in channels is shown in figure 7.

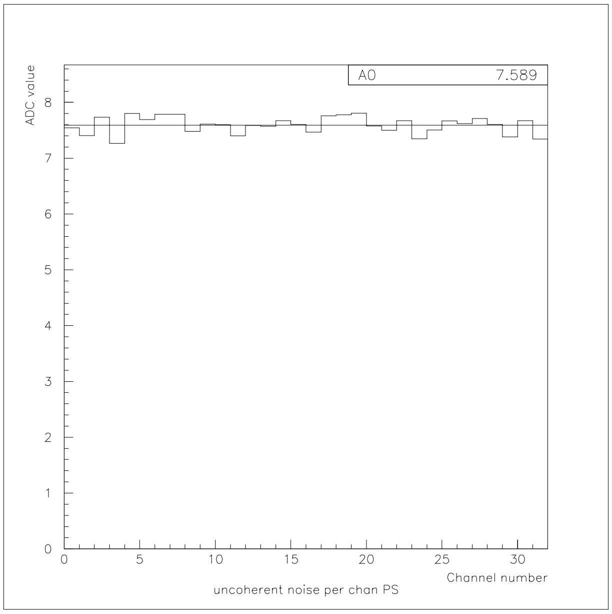

Figure 7: Incoherent noise in channels of presampler.

5 Capacitances and crosstalks

5.1 Capacitances calculation and measurements

Calculated capacitances of the signal pads (figure 8) are presented in table 2. We use the formula $C_{full} = 2 \cdot C_{gap} + C_{edge}$, where

$$C_{gap} = \varepsilon_0 \varepsilon_{LAr} \cdot S/D, \;\; C_{edge} = \alpha_{edge} \cdot P,$$

$\varepsilon_{LAr} = 1.54$ is LAr dielectric constant, S and P are the surface area and the perimeter of the read-out cell, respectively, $D = 2\,mm$ is the gap size. The coefficient α_{edge} was measured to be $0.5\,pF/cm$.

η	P,cm	S, cm^2	C_{edge}	C_{gap}	C_{full}
1.500-1.525	42.2	76.2	21.1	51.9	125.1
1.525-1.550	41.0	71.8	20.5	49.0	118.4
1.550-1.575	39.9	67.7	19.9	46.1	112.2
1.575-1.600	38.8	63.8	19.4	43.5	106.4
1.600-1.625	37.7	60.2	18.9	41.1	100.9
1.625-1.650	36.7	56.8	18.3	38.7	95.8
1.650-1.675	35.7	53.6	17.8	36.5	90.9
1.675-1.700	34.7	50.7	17.3	34.5	86.4
1.700-1.725	33.8	47.9	16.9	32.6	82.1
1.725-1.750	32.8	45.2	16.4	30.8	78.0
1.750-1.775	32.0	42.8	16.0	29.2	74.3
1.775-1.800	31.1	40.4	15.6	27.6	70.7

Table 2: The calculated capacitances (pF) of read-out cells

Calculated capacitance from HV layer to the ground is 5.3 nF, the measured value is 5.5 nF. Calculated (using ANSYS code [11]) and measured capacitances between different pads are presented in table 3. The capacitance between cell number i and cell number j (the

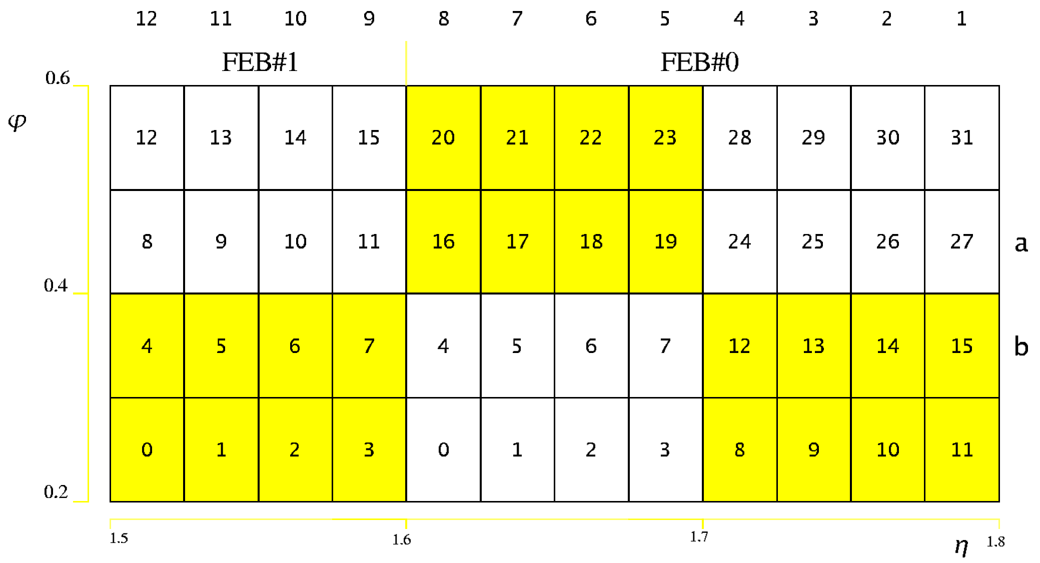

	12	11	10	9	8	7	6	5	4	3	2	1	
	12	13	14	15	20	21	22	23	28	29	30	31	
	8	9	10	11	16	17	18	19	24	25	26	27	a
	4	5	6	7	4	5	6	7	12	13	14	15	b
	0	1	2	3	0	1	2	3	8	9	10	11	

Figure 8: Presampler layout.

numeration is presented on top of the figure 8) with equal ϕ position is denoted as $a_i a_j$ while the capacitance between cell number i and cell number j in adjacent row in ϕ is designated as $a_i b_j$. The information about capacitances between different cells was used for estimation of the crosstalk in calibration runs (see section 5.3). The capacitance values not listed in table 3, were approximated within a simplified model:

1. If ϕ positions of the pads differ by more than 1 then the capacitances between these pads are equal to zero.
2. Capacitance values between the pads with equal ϕ positions $a_i a_j$ (j>i) are equal to $a_1 a_{j-i+1} \cdot \frac{a_i a_{i+1}}{a_1 a_2}$.
3. Capacitance values between the pads with ϕ positions differing by 1 $a_i b_j$ (j>i) are equal to $a_i a_j \cdot \frac{a_i b_{i+1}}{a_i a_{i+1}}$.

For example, we substitute $a_2 a_5 = a_1 a_4 \cdot \frac{a_2 a_3}{a_1 a_2}$, $a_3 b_5 = a_1 a_3 \cdot \frac{a_3 b_4}{a_1 a_2}$ etc.

$Pads$	C_{calc}	C_{meas}	$Pads$	C_{calc}	C_{meas}	$Pads$	C_{meas}	$Pads$	C_{meas}
$a_1 a_2$	6.2	6.7	$a_1 b_1$	2.0	2.3	$a_1 b_2$	2.0	$a_1 a_2$	6.7
$a_2 a_3$	6.4	6.9	$a_2 b_2$	2.1	2.7	$a_2 b_3$	2.2	$a_1 a_3$	3.0
$a_3 a_4$	6.6	7.2	$a_3 b_3$	2.2	3.0	$a_3 b_4$	2.4	$a_1 a_4$	1.7
$a_4 a_5$	6.8	7.5	$a_4 b_4$	2.2	3.2	$a_4 b_5$	2.5	$a_1 a_5$	1.1
$a_5 a_6$	6.9	7.8	$a_5 b_5$	2.3	3.4	$a_5 b_6$	2.7	$a_1 a_6$	0.75
$a_6 a_7$	7.1	8.1	$a_6 b_6$	2.4	3.5	$a_6 b_7$	2.8	$a_1 a_7$	0.55
$a_7 a_8$	7.4	8.3	$a_7 b_7$	2.4	3.65	$a_7 b_8$	3.0	$a_1 a_8$	0.4
$a_8 a_9$	7.7	8.6	$a_8 b_8$	2.5	3.75	$a_8 b_9$	3.1	$a_1 a_9$	0.28
$a_9 a_{10}$	7.9	8.8	$a_9 b_9$	2.7	3.85	$a_9 b_{10}$	3.3	$a_1 a_{10}$	0.21
$a_{10} a_{11}$	8.2	9.1	$a_{10} b_{10}$	2.8	3.95	$a_{10} b_{11}$	3.4		
$a_{11} a_{12}$	8.4	9.3	$a_{11} b_{11}$	2.9	4.05	$a_{11} b_{12}$	3.2		
			$a_{12} b_{12}$	3.0	3.7				

Table 3: Calculated and measured capacitances (in pF) between different pads. The cell numeration is presented in figure 8.

5.2 Crosstalk in the model circuit

The crosstalk between two neighbouring presampler pads was calculated for an equivalent circuit taking into account the parameters of the presampler electronic circuit and the capacitance values. The results are shown on figure 9. The peak-to-peak crosstalk measured in the test bench (1.5% of signal) is in agreement with calculated one (2.0% of signal). The crosstalk due to the capacitance from one readout strip line to another is 30 times smaller than the crosstalk due to the capacitance between the pads.

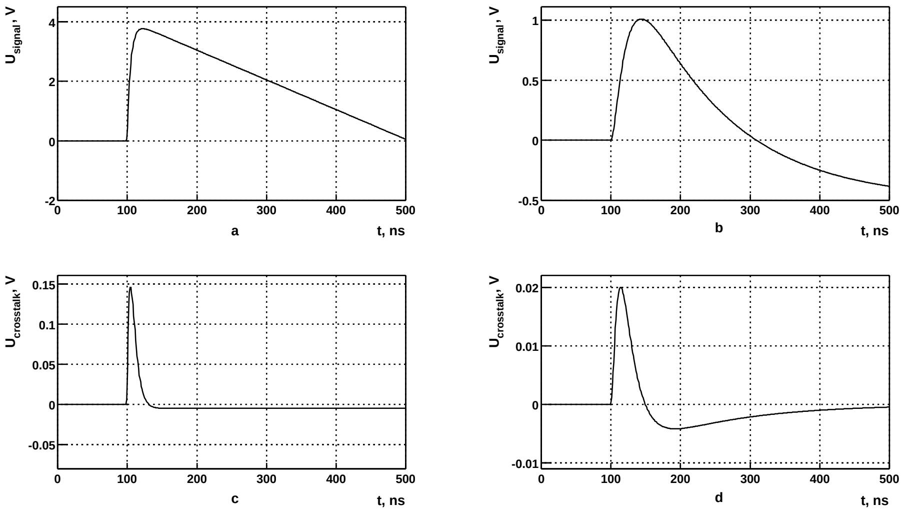

Figure 9: Simulated crosstalk in equivalent circuit: (a) signal on pad, (b) signal on pad after shaping, (c) crosstalk on neighbouring pad, (d) crosstalk on neighbouring pad after shaping.

5.3 Crosstalk in calibration runs

For this measurement we used calibration delay runs, where signals from generator with constant DAC value were simultaneously injected into 3 groups of 8 channel (highlighted areas on figure 8). Typical calibration signal in one channel and crosstalk signal in channel #0 of FEB #0 is shown in figures 10a and 10b respectively.

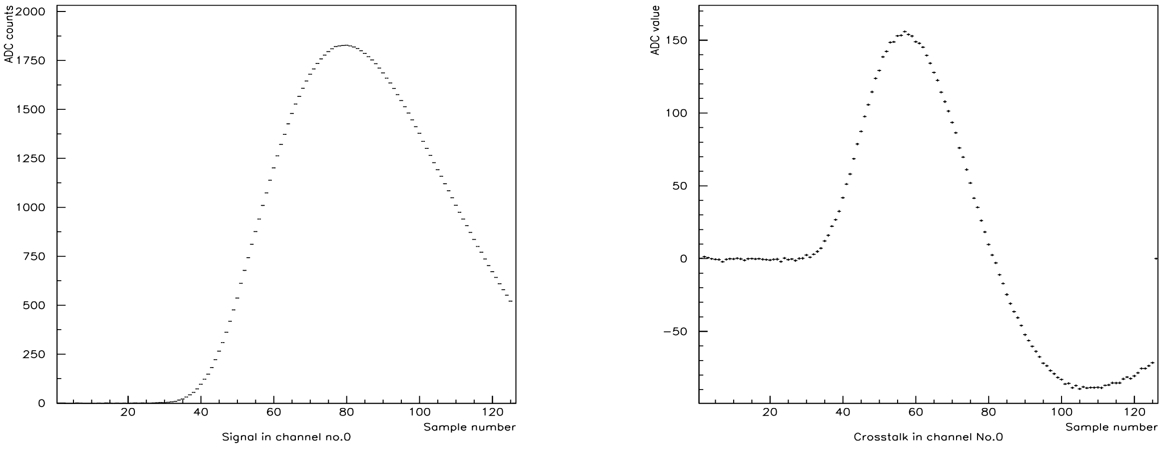

a b

Figure 10: Typical calibration signal in one channel (a), crosstalk in channel #0 from calibration signal (b).

The signal near the peak was fit by parabolic function. Parameters obtained from the fit were used to get the peak position and amplitude of the crosstalk signal. All results of fits are shown in table 4 (signal) and 5 (crosstalk).

#	DAC = 100		DAC = 500		DAC = 1000	
	peak pos.	signal amp.	peak pos.	signal amp.	peak pos.	signal amp.
0	83.11±0.24	177.9±4.6	81.77±0.04	891.0±4.6	81.36±0.02	1782.6±4.5
1	82.70±0.22	184.5±4.5	81.14±0.05	922.4±4.5	80.72±0.02	1845.8±4.6
2	82.72±0.21	184.5±4.5	81.35±0.04	919.2±4.4	80.93±0.02	1838.5±4.5
3	83.02±0.23	182.6±4.6	81.67±0.04	914.5±4.5	81.25±0.02	1828.9±4.6
4	82.99±0.22	182.8±4.7	81.51±0.05	913.2±4.7	81.05±0.02	1827.7±4.8
5	82.73±0.21	184.1±4.5	81.29±0.04	917.3±4.4	80.85±0.02	1835.2±4.7
6	82.50±0.22	185.7±4.0	81.32±0.04	927.9±4.6	80.92±0.02	1855.8±4.8
7	83.34±0.22	189.3±4.8	82.06±0.04	943.7±4.7	81.71±0.02	1887.0±4.7

Table 4: Parameters of signal peak for channels # 0 – 7 for FEB #0.

#	DAC = 100		DAC = 500		DAC = 1000	
	peak pos.	signal amp.	peak pos.	signal amp.	peak pos.	signal amp.
0	60.2±1.0	15.0±3.6	59.30±0.19	75.5±3.8	58.80±0.09	150.2±3.7
1	59.9±1.0	13.8±3.7	58.70±0.21	70.0±3.9	58.29±0.10	139.6±3.9
2	60.6±0.9	14.0±3.6	58.92±0.20	70.0±4.0	58.42±0.10	139.1±3.9
3	60.7±0.9	16.4±3.6	59.29±0.18	79.3±3.8	58.86±0.09	159.1±3.9
4	59.0±0.7	20.8±3.7	57.66±0.15	103.9±3.8	57.16±0.08	207.7±3.8
5	58.7±0.8	20.1±3.6	57.66±0.15	101.4±3.8	57.13±0.08	201.5±3.8
6	59.4±0.7	18.7±3.7	57.88±0.16	93.2±3.8	57.43±0.08	186.3±4.0
7	60.2±0.7	22.3±3.7	58.82±0.14	111.4±3.9	58.37±0.07	221.9±4.0

Table 5: Parameters of the peak of crosstalk signal.

The dependence of signal and crosstalk amplitudes on DAC code of calibration generator was fit by linear function. Using DAC/ADC ratio founded in section 4.1, we can get the ratio between the value of crosstalk signal and the value of calibration signal. This ratio is presented in table 6 for channels $0 \div 7$ of FEB #0.

$Ch\#$	0	1	2	3	4	5	6	7
$meas.$	8.3 ± 0.3	7.6 ± 0.3	7.6 ± 0.3	8.7 ± 0.3	11.3 ± 0.3	11.0 ± 0.3	10.2 ± 0.3	12.0 ± 0.3
$calc.$	7.4	4.8	4.6	6.4	9.9	7.7	7.6	8.7

Table 6: The measured and calculated crosstalk,% in delay runs

We can estimate the values of crosstalk from capacitances between the pads in the presampler, which were measured in section 5.1. Crosstalk between different channels is proportional to capacitance between the corresponding pads. The resulting crosstalk in one cell is the sum of crosstalks from all cells with signal. In the case of calibration signal the crosstalk in each unhighlighted cell is the sum of crosstalk signals from all highlighted cells. So, for total crosstalk signal estimation we have to sum up capacitances between one pad and all corresponding pads for cells with signal. For example, for cell number 0 of FEB #0 (see figure 8)

$$\begin{aligned} C_0 &= a_1a_5 + a_2a_5 + a_3a_5 + a_4a_5 + a_5a_9 + a_5a_{10} + a_5a_{11} + a_5a_{12} + \\ &+ a_1b_5 + a_2b_5 + a_3b_5 + a_4b_5 + a_5b_9 + a_5b_{10} + a_5b_{11} + a_5b_{12} \end{aligned}$$

Taking the values of capacitances between presampler pads from section 5.1, we get crosstalk capacitances:

$$\begin{array}{llll} C_0 = 25.9\,pF & C_1 = 16.9\,pF & C_2 = 16.1\,pF & C_3 = 22.5\,pF \\ C_4 = 34.6\,pF & C_5 = 27.6\,pF & C_6 = 26.4\,pF & C_7 = 30.5\,pF \end{array}$$

It is calculated, that crosstalk in one cell from neighbouring cell with equal ϕ is about 2% (figure 9). It corresponds to crosstalk capacitance of about $7\ pF$. So, we can estimate total crosstalk signal A_i from capacitances ratio: $A_i = 0.02 \cdot \frac{C_i\ (pF)}{7\ pF}$, where A_i is the crosstalk value in units of calibration signal. The final results of calculations are compared with measurements in table 6. The calculated signal is smaller than the measured one. One can explain the discrepancy in results by possible uncertainty in capacitances measurement and some uncertainty of our assumptions.

5.4 Crosstalk in physics runs

In calibration, the position of the signal maximum slightly depends on signal amplitude and corresponds approximately to 80th time sample (figure 10a). At this time crosstalk signal is close to zero (figure 10b). So, from this fact we could conclude that crosstalk signal has no influence on reconstructed signal value. But there is some difference between calibration and physics signals. The equivalent electrical circuits in these cases differ: in calibration the current pulse from generator goes directly to the ground while in physics the current signal from presampler goes to the ground through the cell capacitance. It changes the shape of the crosstalk signal (figure 11).

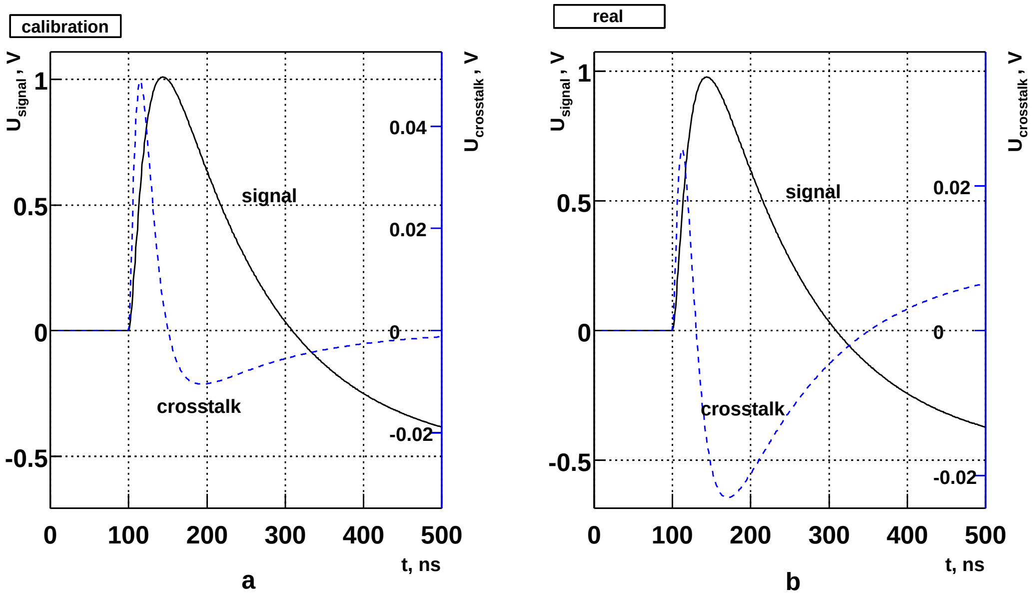

Figure 11: Signal and crosstalk signal in calibration case (a) and in physics case (b).

For crosstalk observation in physics events, the run in which 100 GeV electron beam was pointed at the center of the cell #29 (figure 8) was chosen (run #103865). There were in total 2 X_0 of dead material in front of the presampler.

Crosstalk measurement was based on the following idea. In this run the energy deposition in cell #29 was 10 times larger than in any other presampler cell. So the main crosstalk originates in this channel. We can consider the dependence of energy deposition in neighbouring to the most energetic cell (e.g. #28 or #30) on energy deposition in this cell (#29). In presence of crosstalk between presampler channels, this dependence in data will be different than in simulation without crosstalk by linear function of energy deposited in most energetic presampler cell. Here we assume that only the signal from the most energetic cell produces crosstalk and this crosstalk linearly depends on signal amplitude. Then the difference in coefficients of linear fit of this dependence for physics events and simulated ones gives the value of crosstalk. This method was tested and gave good results on simulated events, with included crosstalk between channels.

For event selection we used the same standard criteria as in analysis of energy resolution (see section 6). As the beam had wide spatial shape, information about the coordinates measured in the calorimeter was used to select events, where the beam hits the central part of the cell. In figure 12 dependences of energy deposition in channel #30 versus channel #29 are shown for simulation without crosstalk (a) and for experiment (b).

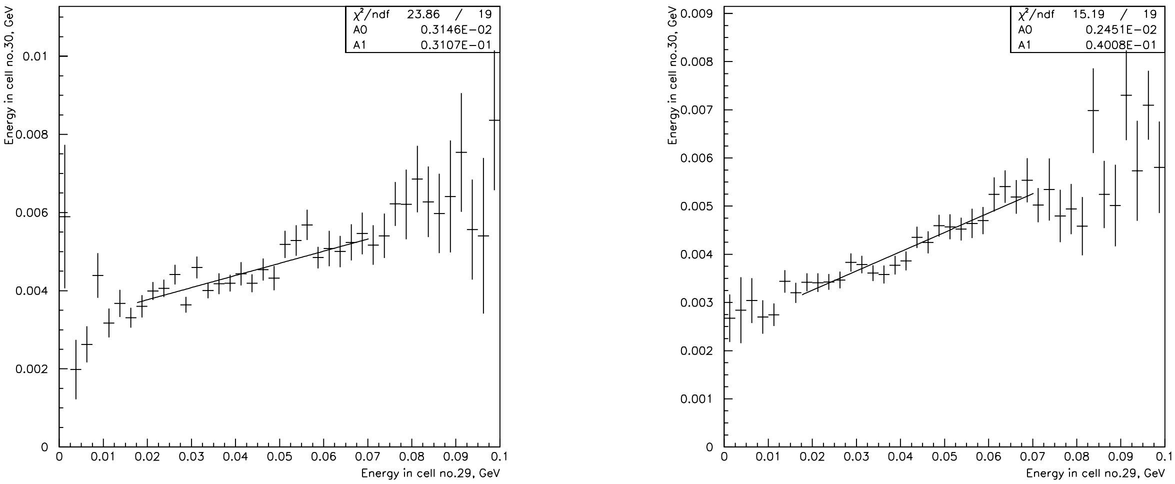

a

b

Figure 12: Dependence of energy deposition in channel #30 on energy deposition in channel #29 in simulation without crosstalk (a) and in experiment (b).

Using fit result we found crosstalk value in neigbour channels as well as statistical error of fit.

$$
\begin{aligned}
\#30: &\quad 0.9\% \pm 0.5\% \\
\#28: &\quad 0.8\% \pm 0.5\%
\end{aligned}
$$

For all other channels the crosstalk value is substantially lower than statistical errors. So, crosstalk at the level of 1% was observed for neigbouring channels with the same ϕ coordinate.

6 Algorithm of energy reconstruction

Following cuts and algorithms were selected for energy reconstruction :

- Particle type selection to reject muon, pion and random events.
- Standard EMTB-1-3 framework [10] with *parabola* method for evaluation of signal amplitude was used. In ATLAS-like electronics [2] for each channel 3 output signals with amplification factor ratio about 1/10/100 (low, medium and high gain) are simultaneously digitized. In presampler and in calorimeter back section using of high gain is sufficient. In strips and in middle sampling *the software free gain* was used (the medium gain was taken in the case of saturation of the high gain in particular channel).
- The cluster was constructed around the most energetic cell in middle sampling. Number of cells included in cluster for each sampling is shown in table below. In order to get better compromise between transverse shower leakage fluctuations and electronics noise we used larger cluster size (cluster 2) for runs with presence of additional dead material in front of the calorimeter.

$Dead\ \ material$	$Presampler$	$Strip\ (S_1)$	$Middle\ (S_2)$	$Back\ (S_3)$	
$1.7\ X_0$	$3 \times 1(2)$	$24 \times 1(2)$	3×3	1×1	$Cluster1$
$1.7 < X_0 \leq 4.9$	3×2	40×2	5×5	1×1	$Cluster2$

  The values in brackets indicate the cluster size when the beam impact point is close to the edge of corresponding cell. The clucter size in back section was reduced in order to diminish the contribution of inductive cosstalk from middle section, caused by insufficient grounding in summing and motherboards [12]. Note, that back sampling was not used at all for $E_{beam} < 50\ GeV$ (like in TDR [13] analysis).
- Cut on impact point determined as (ϕ, η) barycenters in middle sampling.
  $\eta_{bary} \in [\overline{\eta_{bary}} \pm 0.5], \quad \phi_{bary} \in [\overline{\phi_{bary}} \pm 0.5],$
  where η_{bary}, ϕ_{bary} are barycenters for current event in terms of cell number, $\overline{\phi_{bary}}$,$\overline{\eta_{bary}}$ - their averages over all events in the run.
- High voltage correction. For $S_{1,2,3}$ special weights depending on η_{cell} were applied to each cell amplitude as described in [14].
- For runs with dead material additional correction was applied (see section 8) to account for the energy lost in front of the accordion.
- η, ϕ, $time(TDC)$ - corrections
  The last correction was necessary because the trigger in experiment was asynchronous with respect to the 25 ns sampling clock.

For simulation the same algorithm was used, except for unneeded particle type selection and time correction.

6.1 Global scale factor

For runs without dead material energy deposition in calorimeter is $E_{tot} = E_{S_1} + E_{S_2} + E_{S_3}$, where E_{S_i} is the cluster energy for sampling i. The cell energy in the sampling i is:

$$E_{S_1} = \gamma \times \frac{1}{6} \times DAC, \;\; E_{S_2} = \gamma \times DAC, \;\; E_{S_3} = \gamma \times \frac{1}{2} \times DAC$$

Global calibration factor γ was calculated as the ratio of the beam energy to the mean of the signal distribution for $60\ GeV$ run without additional dead material. For two cluster sizes used in the analysis (see table in previous subsection) following values were obtained:

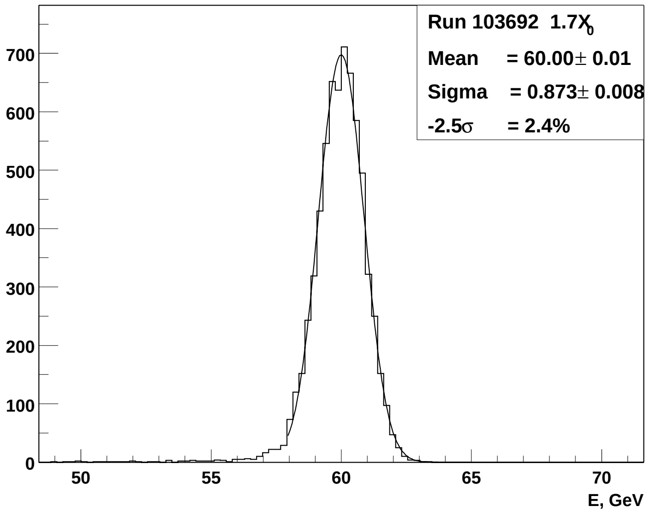

Figure 13: Energy distribution for 60 GeV run, $1.7X_0$, cluster size 3×3.

$\gamma_1 = 0.03247$ for *cluster 1* and $\gamma_2 = 0.03003$ for *cluster 2* which was used for runs with additional dead material.

Figure 13 shows E_{tot} distribution for 60 GeV run, Point 3, $1.7\ X_0$ and cluster size "3×3" after applying of the global calibration factor.

7 Energy deposition in calorimeter sections

7.1 Energy spectra in presampler

Figure 14a shows energy spectra in presampler cluster at beam energy of 40 GeV for different values of X_0. The first distribution is obtained for random events, the others for physics events. For example with extra material of 1.82 X_0 (in total 3.5 X_0) average energy in presampler is about 50 MeV whereas presampler cluster noise obtained from random events is about 5 MeV, which is consistent with the measured value of noise in single presampler cell of 2.8 MeV. The second histogram shows the dependence of average presampler energy on the beam energy for different values of X_0 in simulation and experiment.

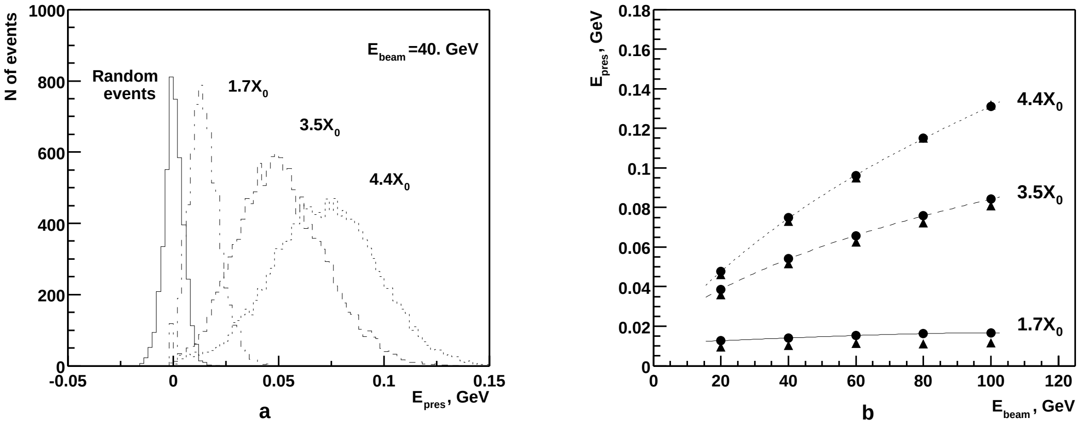

Figure 14: Energy in presampler for 3 values of amount of upstream dead material.
a) energy spectra, b) average energy, ● - experiment, ▲ - simulation.

7.2 Comparison of energy spectra in simulation and experiment

Energy spectra in samplings for simulation (filled histrograms) and experiment (open histograms) for 40 GeV, $1.7X_0$ run are shown on figure 15. The global scale was applied in order to get the correct value of the mean energy.

It is seen, that energy spectra in back section strongly differ due to high value of inductive crosstalk from middle section in experiment [12]. There are also discrepancies between simulation and experiment in strip and middle section. Mean energy in strip section is bigger in experiment than in simulation, in middle section vice versa. One possible reason is not sufficient amount of dead material described in simulation. The exact position of supporting zigzag structure situated between cryostat walls (see figure 4) is not known. Its contribution could be up to 0.15 X_0 (figure 5). The realistic description of material in calorimeter motherboards adds about 0.05 X_0 [15]. But adding 0.2 X_0 in simulation does not completely remove the discrepancy: the difference of average energy depositions in experiment and in simulation in strip section becomes +1.03 GeV instead of +1.7 GeV, while in middle section -1.39 GeV instead of -2.21 GeV. The other possible reason of the discrepancy between experiment and simulation is bad functionality of parabola method at small amplitudes which leads to overestimating of energy measured in cells in experiment. This effect amounts to 30 MeV/cell in strip section and 64 MeV/cell in back section (these numbers are relevant only for cells where the energy deposition does not exceed several rms of electronics noise). The rms of electronics noise is about 20 MeV/cell and 40 MeV/cell respectively. In total the bias introduced by using the parabola method is estimated to be 0.5 GeV in strip section and 0.25 GeV in back section for cluster size 3x3. Finally, even after applying both corrections described above, some discrepancy between simulation and experiment in mean energy deposition in samplings still remains.

Figure 16 shows energy spectra for 40 GeV, 4.4 X_0 run. The agreement between simulation and experiment is better. Obviously both factors discussed above (possible lack of material described in simulation and the bias of parabola method at small amplitudes in experiment) here are less significant. Table 7 shows the summary of average energy deposition in samplings in simulation and in experiment.

X_0	E, GeV	Pres		Strip		Middle		Back	
		exp	sim	exp	sim	exp	sim	exp	sim
1.7	20	0.068	0.055	31.17	25.92	68.02	73.12	0.749	0.887
	40	0.037	0.029	24.75	20.41	73.91	79.01	1.291	0.541
	100	0.017	0.013	17.49	14.55	80.9	84.74	1.57	0.676
3.5	20	0.204	0.183	44.56	40.75	54.3	58.11	0.756	0.959
	40	0.141	0.129	38.72	35.36	59.94	64.08	1.103	0.427
	100	0.088	0.079	30.9	28.42	67.73	71.1	1.173	0.389
4.4	20	0.292	0.269	49.22	45.91	49.52	52.63	0.793	1.168
	40	0.218	0.202	44.21	41.14	54.4	58.17	1.055	0.431
	100	0.147	0.138	36.8	34.7	61.81	64.81	1.047	0.311

Table 7: Mean energy deposition in samplings in % of total energy. Simulation and experiment.

7.3 Energy deposition in dead material (simulation)

Mean and RMS of energy deposition in dead material for different beam energies and total amount of upstream dead material are given in table 8.

Figure 17a shows the dependence of energy deposited in front of the active part of the accordion E_{dead} on beam energy for different values of X_0. The dependence of E_{dead} on presampler energy E_{pres} and the distribution over their ratio for beam energy 100 GeV and 4.4 X_0

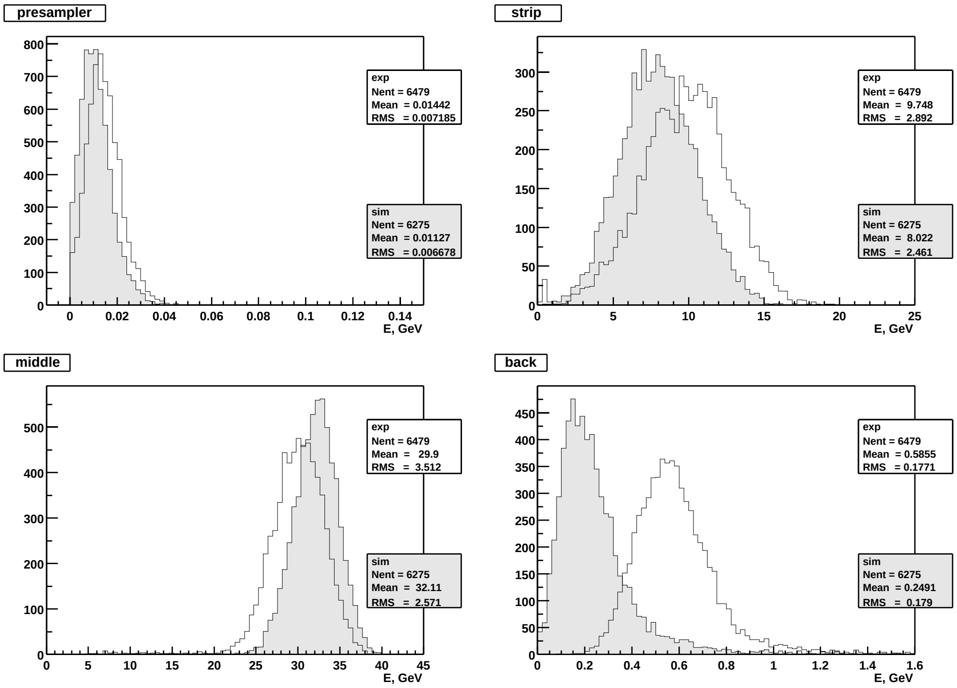

Figure 15: Energy distributions in calorimeter sections for 40 GeV runs without additional dead material. Open histograms- experiment, full histograms- simulation.

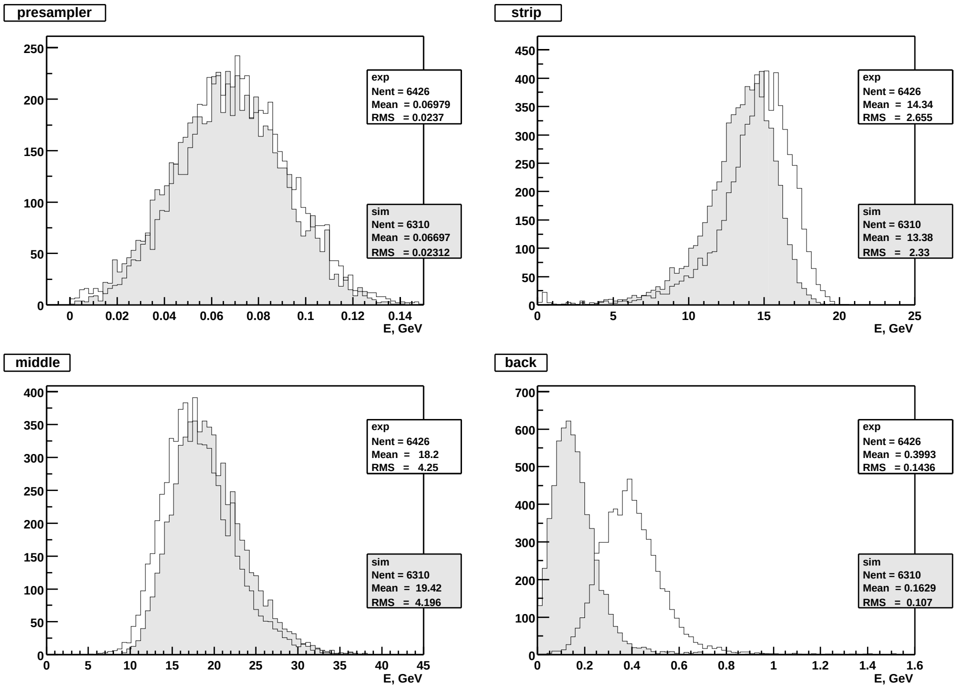

Figure 16: Energy distributions in calorimeter sections for 40 GeV runs with $2.7X_0$ of additional upstream material. Open histograms- experiment, full histograms- simulation.

E_{beam}	$20GeV$	$40GeV$	$60GeV$	$80GeV$	$100GeV$
t	$mean\ \ rms$	$mean\ \ rms$	$mean\ \ rms$	$mean\ \ rms$	$mean\ \ rms$
$1.7\ X_0$	$0.38\ \ 0.18$	$0.48\ \ 0.22$	$0.55\ \ 0.25$	$0.59\ \ 0.27$	$0.65\ \ 0.30$
$3.5\ X_0$	$2.38\ \ 0.86$	$3.40\ \ 1.24$	$4.17\ \ 1.55$	$4.80\ \ 1.76$	$5.35\ \ 2.01$
$4.4\ X_0$	$3.79\ \ 1.04$	$6.05\ \ 1.91$	$7.82\ \ 2.57$	$9.27\ \ 3.04$	$10.49\ \ 3.50$

Table 8: Energy deposition (GeV) in dead material.

is shown on figure 17b,17c. Figure 17d shows the average value of the ratio E_{dead}/E_{pres} versus beam energy for different values of X_0. Good linearity seen in figure 17b means that the signal in presampler is proportional to the energy lost in the upstream dead material.

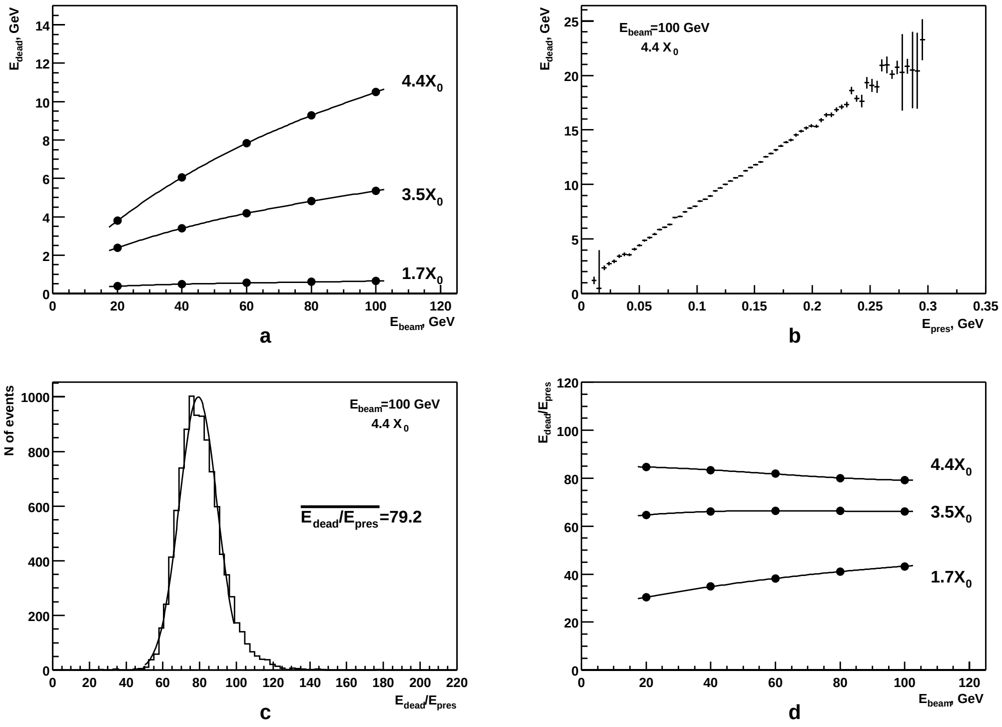

Figure 17: Simulation: a - energy deposition in dead material, b - dependence of the energy loss in dead material in front of the active part of the accordion on presampler energy, c - distribution over the ratio E_{dead}/E_{pres}, d - dependence of E_{dead}/E_{pres} on beam energy for different values of X_0. b,c - for electrons E $= 100$ GeV and total amount of upstream material before the active part of the calorimeter 1.7+2.7 X_0.

8 Energy reconstruction in presence of dead material

For runs taken in presence of dead material three different algorithms of energy reconstruction were studied.

1) Only presampler weight is optimised. (section 8.1)
Energy deposition is the sum of energy in presampler multiplied by weight α_{pres} and energy in calorimeter calculated as usual.

$$E_{tot} = \alpha_{pres} \cdot E_{pres} + \sum_{i=1}^{3} E_{S_i}$$

Presampler weight was varied in order to minimize the energy resolution.
2) Combined optimization of presampler and sampling weights (section 8.2)

$$E_{tot} = \alpha_{pres} \cdot E_{pres} + \sum_{i=1}^{3} \alpha_i \cdot E_{S_i}$$

Presampler weight α_{pres} and sampling weights $\alpha_{1,2,3}$ are derived together from requirement of minimum of $\overline{(E - \overline{E})^2}$ over all selected events.
3) Presampler is not used at all, only sampling weights are optimised. (section 8.3)
The same as in previous case, but only $\alpha_{1,2,3}$ were varied to get best resolution and recover the energy lost in dead material.

8.1 Optimization of presampler weight

In this approach the weights for strip, middle and back samplings remained the same as in runs without additional dead material ($\alpha_{1,2,3} = 1.$) and only presampler weight was varied in order to minimize the energy resolution. Figure 18a shows the dependence of the resolution on presampler weight for 60 GeV, 3.5 X_0 run. Optimal presampler weight equals 69.6 (minimum of parabola), with errors ± 2.4.

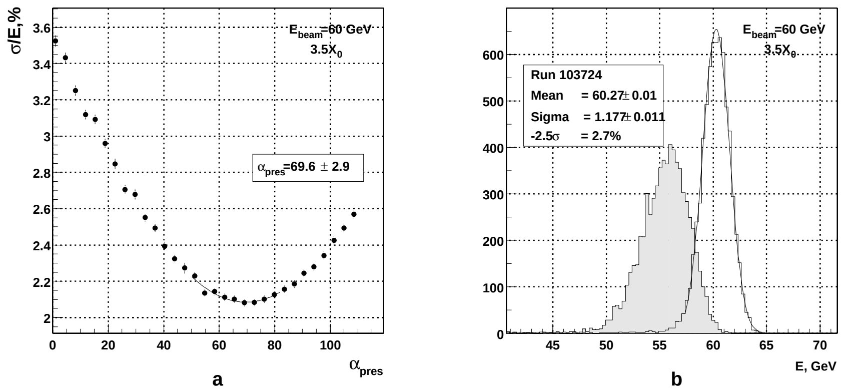

Figure 18: Run #103724, 60 Gev, 3.5 X_0. a) Energy resolution σ_E/E, % versus presampler weight b) Distributions over reconstructed energy for presampler weight=0. (filled histogram) and optimal presampler weight=69.6 (open histogram).

Figure 18b presents two distributions: the energy reconstructed with using the presampler with optimal weight value taken from left picture and without using the presampler. It is seen that applying the optimal presampler weight considerably improves the energy resolution and restores the mean value of total energy.

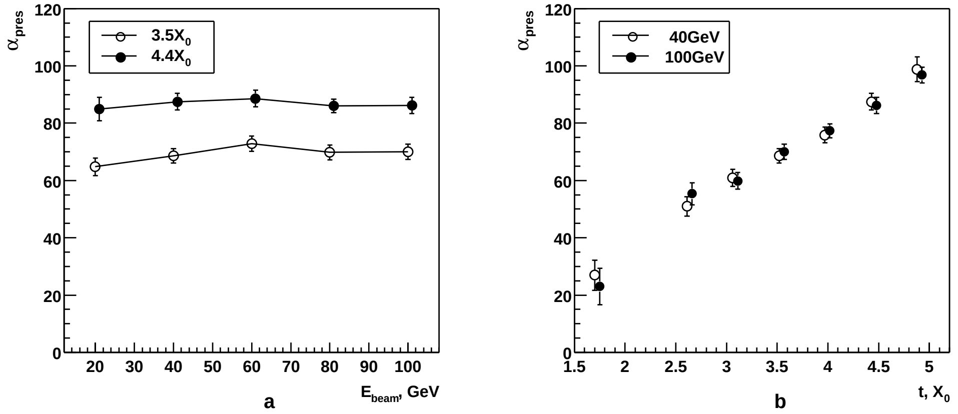

Figure 19: Dependence of optimal presampler weight on energy (a) and total amount of upstream dead material t (b).

The optimal presampler weights were obtained for each value of energy and amount of dead material. Dependence of optimal α_{pres} on energy for two values of total amount of dead material before active accordion ($t = 3.5\ X_0$ and $t = 4.4\ X_0$) is shown on figure 19a. Figure 19b shows the dependence of optimal α_{pres} on $t\ [X_0]$. It is seen that optimal values of α_{pres} are close to corresponding values of E_{dead}/E_{pres} presented in figure 17d.

No obvious dependence on E_{beam} was observed. In following analysis we have used for presampler weight the formula $\alpha_{pres} = 19.6 \cdot t\ [X_0]$ for all energies. No difference was observed for optimal presampler weights obtained for Point 3 (the center of presampler cell) and for Point $4'$ (the intersection of presampler cells).

Figure 20a shows the energy resolution for beam Point 3 and $t = 1.7, 3.5, 4.4 X_0$. Beam energy spread is already subtracted (see Appendix 2 for details). Figure 20b shows the linearity of reconstructed energy versus E_{beam} for the same cases. It is seen that in the entire energy range of $40 \div 100$ GeV the linearity is better than 2 %. The drop in linearity is observed for $E_{beam} = 20$ GeV for present algorithm of energy reconstruction.

The parameters of the fit of the resolution in experiment σ_E/E, % by function $p_1/\sqrt{E\,[GeV]} \oplus p_2/E\,[GeV] \oplus p_3$ are presented in table 9.

t	p_1	p_2	p_3
$1.7\ X_0$	8.05 ± 1.28	0.329 ± 0.057	0.89 ± 0.12
$3.5\ X_0$	13.22 ± 0.17	0.545 ± 0.017	0.00 ± 0.62
$4.4\ X_0$	18.16 ± 0.67	0.873 ± 0.062	0.00 ± 0.85

Table 9: The parameters of the fit of energy resolution in experiment by function $\frac{p_1}{\sqrt{E}} \oplus \frac{p_2}{E} \oplus p_3$

t	$20\ GeV$	$40\ GeV$	$60\ GeV$	$80\ GeV$	$100\ GeV$
$1.7\ X_0$	0.186	0.187	0.189	0.202	0.210
$3.5\ X_0$	0.434	0.456	0.473	0.475	0.479
$4.4\ X_0$	0.517	0.534	0.553	0.555	0.544

Table 10: Total cluster noise [GeV] for random events

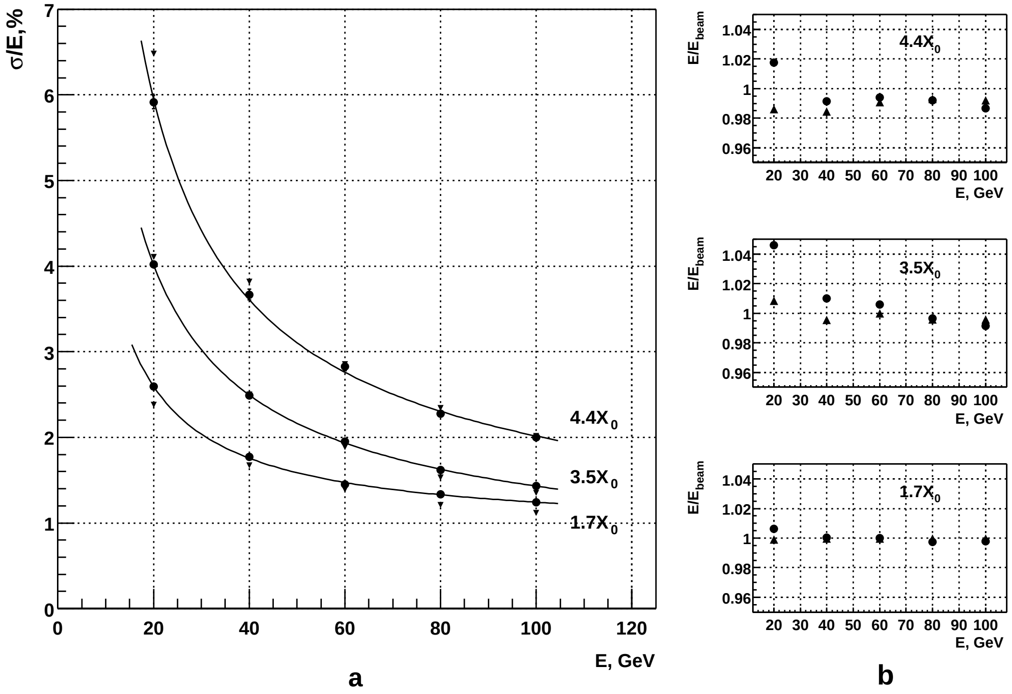

Figure 20: a) Energy resolution versus electron energy for 3 values of total amount of upstream dead material (● - experiment, ▲ - simulation). The curves are results of the interpolation of the resolution in experiment $\frac{\sigma_E}{E}$, % by function $p_1/\sqrt{E\,[GeV]} \oplus p_2/E\,[GeV] \oplus p_3$ (see table 9).
b) energy linearity.

The values of cluster noise obtained from the fit (parameter p_2 in table 9 gives noise value in GeV) should be compared with cluster noise obtained using random events. This noise is quadratic sum of presampler noise multiplied by optimal weight and noise of cluster in the calorimeter:

$$CLS_{noise} = \alpha_{pres} \cdot PRES_{noise} \oplus CALO_{noise}$$

Presampler noise is ~ 5 MeV for 3×2 cluster size. It gives for presampler cluster noise after multiplying by optimal α_{pres} 0.360 GeV (0.460 GeV) for $t = 3.5\,X_0$ ($t = 4.4\,X_0$). Typical value of cluster noise in calorimeter for 5×5 cluster is about 0.290 GeV. Total cluster noise obtained using random events is given in table 10.

There is some discrepancy in cluster noise obtained from the fit and from random events especially for $t = 4.4\ X_0$. The possible reason is not large enough cluster size for low energy and high value of t. Other possible source of discrepancy could be the fluctuations of energy deposition in dead material ($\sim 0.6\,X_0$) between presampler and active part of the calorimeter, which lead to the distortion of the parameters of the fit.

8.2 Combined optimization of presampler and sampling weights

In this most general approach one simultaneously searches for presampler and sampling weights which minimize the energy resolution and satisfy the requirement that the mean value of reconstructed energy is equal to the beam energy.

Figures 21,a-i show the results of such optimization for presampler, strip and middle sections for $t = 3.5\,X_0$ and $t = 4.4\,X_0$. The weight of back section was fixed to be 1.0.

Considering the error bars on plot 21 one has to take into account the strong correlation between sampling weights.

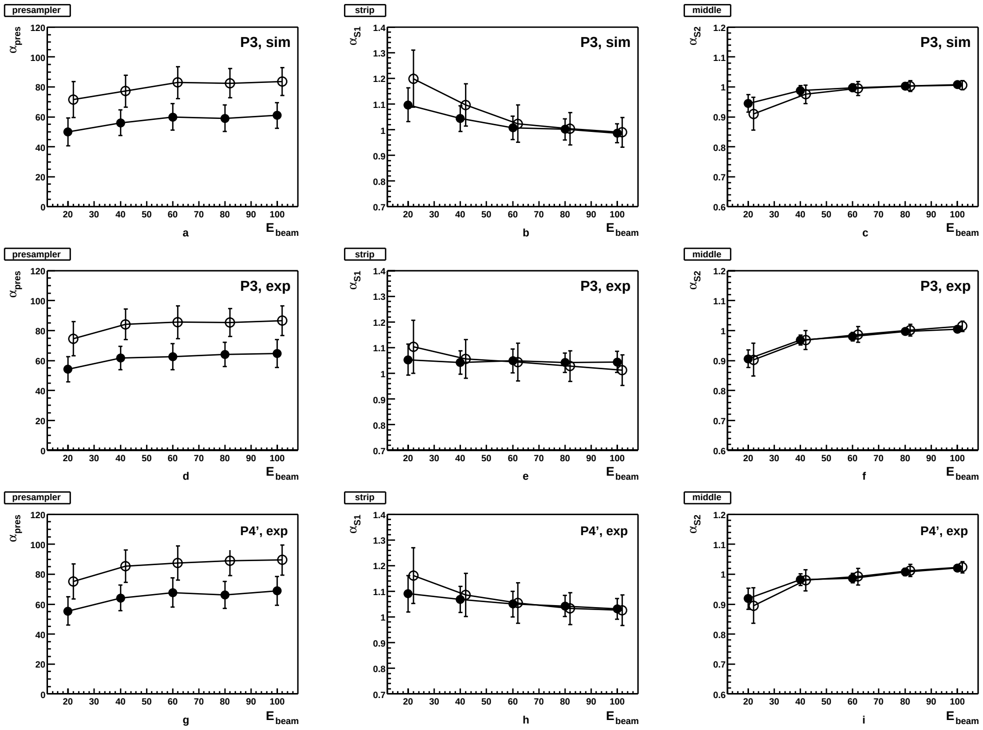

Figure 21: Optimal sampling weights in presence of dead material. a,b,c - Point 3 simulation, d,e,f - Point 3 experiment, i,j,k - Point $4'$ experiment (see the map of points on figure 6).
$\bullet - t = 3.5\,X_0, \circ - t = 4.4\,X_0$

In order to get the sampling weights suitable (at given value of amount of upstream dead material) for any impact point inside the cell, the averaged over points 3 and $4'$ energy dependence for each sampling weight was fit by 3rd order polinomial. Energy resolution for point 3 obtained using the sampling weights derived from this fit is shown on figure 22.

Comparing figure 22 and 20 one can conclude that combined optimization of presampler and sampling weights almost does not improve the energy resolution but improves the energy linearity with respect to the case where only presampler weight is optimized.

The parameters of the fit of the resolution in experiment $\frac{\sigma_E}{E}$, % by function $p_1/\sqrt{E\,[GeV]} \oplus p_2/E\,[GeV] \oplus p_3$ are presented in table 11 (see also table 9 and discussion in the end of previous section).

t	p_1	p_2	p_3
$3.5X_0$	13.32 ± 0.28	0.518 ± 0.030	0.00 ± 0.53
$4.4X_0$	18.36 ± 0.89	0.834 ± 0.082	0.00 ± 0.93

Table 11: Combined optimization of presampler and sampling weights.
The parameters of the fit of energy resolution in experiment by function $\frac{p_1}{\sqrt{E}} \oplus \frac{p_2}{E} \oplus p_3$

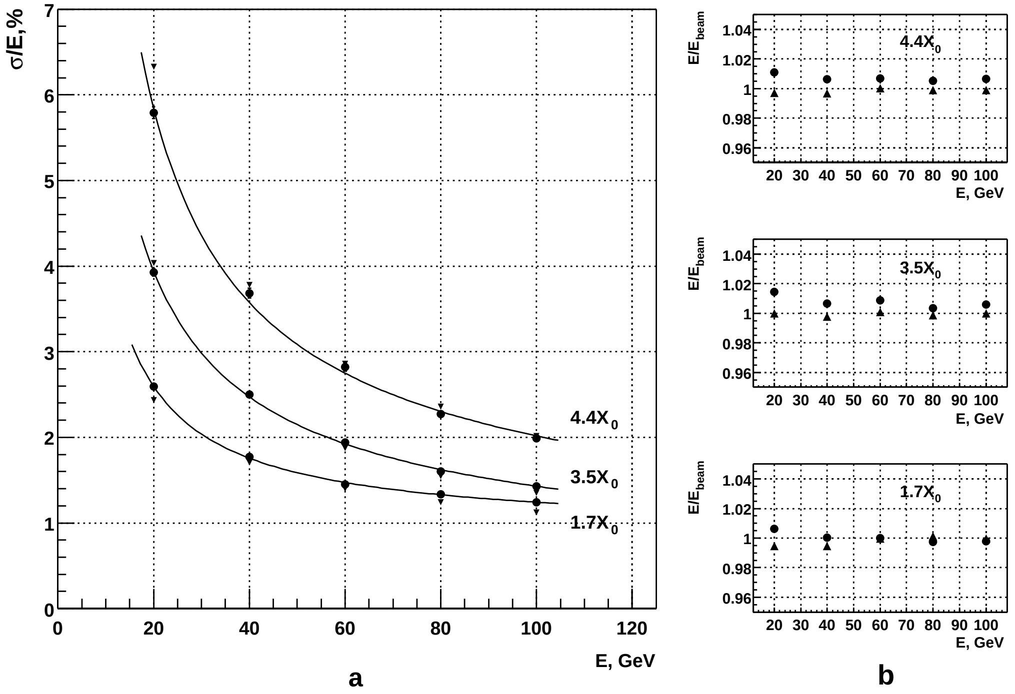

Figure 22: Combined optimization of presampler and sampling weights. a) Energy resolution versus electron energy for 3 values of total amount of upstream dead material (● - experiment, ▲ - simulation). The curves are results of the interpolation of resolution in experiment by function $p_1/\sqrt{E} \oplus p_2/E \oplus p_3$ (see table 11).
b) energy linearity.

8.3 Optimisation of sampling weights while the presampler is not used at all

The energy lost in dead material can be also reconstructed without using the presampler by means of the relative calibration of the strip, middle and back sections. I.e. the special sets of sampling weight coefficients should be used in presence of dead material. One searches for the weights which minimize the energy resolution and satisfy the requirement that the mean value of reconstructed energy is equal to the beam energy.

Figures 23a, 23b shows the results of such optimization for the strip and middle section for energy scan at $t = 3.5\,X_0$ and $t = 4.4\,X_0$. The dependence of optimal weights on X_0 for energy 40 and 100 GeV is shown on figures 23c, 23d. One can derive from figures 23c, 23d that at given value of $t\,[X_0]$ the weights could not be chosen the same for all energies, i.e. the own set of coefficients should be used for each value of t and E_{beam}.

In figure 24 the results for energy linearity (a) and energy resolution (b) are presented for 3 methods: using presampler (in the way described in section 8.1), using a set of optimal sampling weight coefficients without presampler, and without any special correction (default sampling weights are kept). There are only two meaningful curves on plot 24a because for the omitted case (second method) the mean reconstructed energy is equal to the beam energy by definition of optimisation procedure. One can note that without using the presampler the calorimeter performance is much worse.

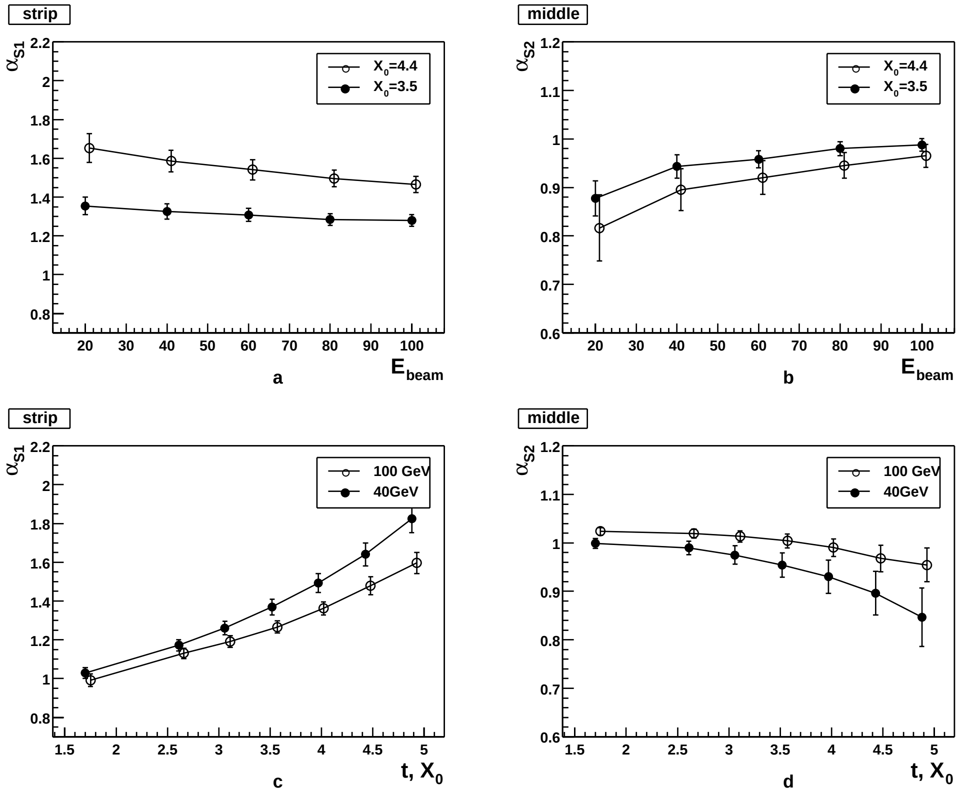

Figure 23: Optimal weights of strip and middle samplings when the presampler is not used. a,b - energy scan, c,d - scan over total amount of upstream dead material $t\,[X_0]$

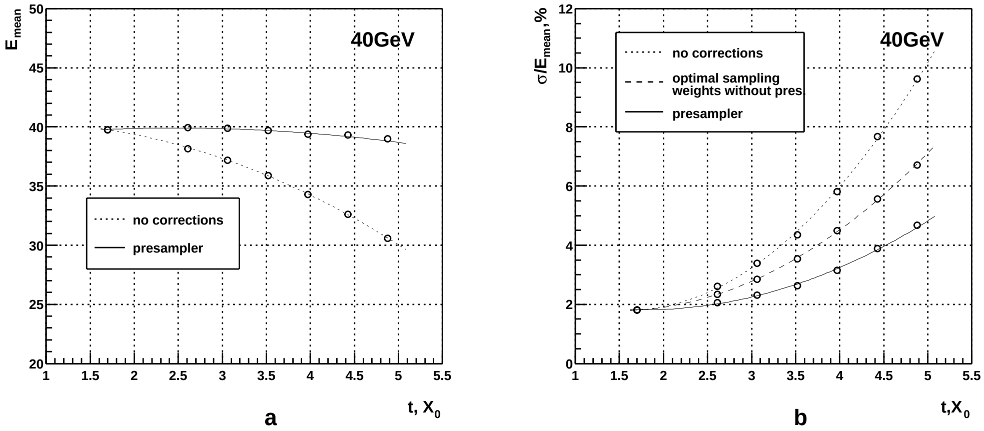

Figure 24: X_0 scan. 40 GeV. Point $4'$. Mean reconstructed energy (a) and energy resolution (b) for three methods: using presampler, using an optimal set of sampling weights without using presampler, and using default sampling weights.

8.4 Comparison of energy resolution at different beam impact points

The results on energy resolution at different beam impact points are presented in table 12. The method described in section 8.1 was used for energy reconstruction. The energy resolution is essentially the same in all three impact points (the center of presampler cell, the intersection of the cells of the same presampler module , the boundary between two presampler modules).

	40 GeV			100 GeV		
$Point$	$1.7\ X_0$	$3.5\ X_0$	$4.4\ X_0$	$1.7\ X_0$	$3.5\ X_0$	$4.4\ X_0$
3	1.77 ± 0.02	2.49 ± 0.03	3.67 ± 0.06	1.24 ± 0.02	1.43 ± 0.02	2.00 ± 0.03
$4'$	1.81 ± 0.02	2.62 ± 0.03	3.89 ± 0.05	1.12 ± 0.04	1.42 ± 0.02	1.97 ± 0.03
$1'$	1.82 ± 0.02	2.65 ± 0.03	3.84 ± 0.07	1.22 ± 0.02	1.41 ± 0.02	1.95 ± 0.03

Table 12: σ/E,% at different beam impact points (see the map on figure 6)

9 Conclusion

This note presents the performance of the end-cap presampler tested at CERN at $20 \div 100$ GeV electron beam together with module 0 of the EM end-cap calorimeter in September-October 1999. The response of the electronic circuit to calibration and physics signals (conversion factors DAC to ADC, ADC to nA, ADC to GeV) as well as the value of electronics noise ($\sigma_{incoh} = 2.7$ MeV/cell) have been measured and found in good agreement with expectations. The peak-to-peak crosstalk between neighbouring presampler cells in calibration runs is about 2 %. In physics the crosstalk value at signal maximum is at the level of 1 %.

It is shown that using the presampler allows one to restore the correct value of mean reconstructed energy and significantly recover the degradation of the energy resolution in presence of upstream dead material. For example, for 40 GeV electrons and 4.0 X_0 before the active part of the calorimeter the energy resolution is 5.81% without corrections, 4.48% for optimal sampling weights but without using the presampler and 3.14% with using the presampler. The results on energy resolution for electrons with energy in the range $20 \div 100$ GeV and various amounts of upstream dead material are obtained and found in agreement with simulation. For up to 4.0 X_0 of upstream material before active part of the calorimeter the linearity of reconstructed energy is better than 2 %. Some discrepancy in energy resolution and energy linearity between experiment and simulation is observed at low energy $E_{beam} = 20$ GeV and large amount of upstream dead material $t \geq 4.0\,X_0$. There is also discrepancy in mean energy depositions in the strip and middle sections of the calorimeter (more energy in strips in experiment). This discrepancy decreases with increasing the amount of upstream dead material or beam energy.

The presampler performance is practically independent on the beam impact point (whether it is the center of cell, the intersection point of the cells of the same presampler module or the boundary between two presampler modules).

Acknowledgments

We would like to thank Pascal Pralavorio for carefully reading this note and for a lot of useful remarks.

References

[1] ATLAS collaboration, *Detector and Physics performance Technical Design Report*, CERN/LHCC/99-14, fig. 4-iii and 4.9.

[2] ATLAS collaboration, *ATLAS Liquid Argon Calorimeter Technical Design Report*, CERN/LHCC/96-41, p.248.

[3] G. Kolachev et al., *EM end-cap presampler. Status report*, 1998, see http://pospelov.home.cern.ch/pospelov/epsm/

[4] G.E. Pospelov, *Performance of the EM end-cap presampler in the Module 00 1998 run*, testbeam meeting March 1999.

[5] K. Elsener, *Short Introduction to the use of the H6 beam*, http://sl.web.cern.ch/SL/eagroup/beams.html#h6

[6] A. Mirea, *Optimisation d'un calorimetre bouchon pour l'experience ATLAS et etude des modeles SUGRA avec violation de la R-parite (Couplage a 3 leptons) avec le detecteur ATLAS*, Ph.D thesis, CPPM-T-1999-02.

[7] J.Y. Hostachy, B. Belhorma, J. Collot, *Performance and characteristics of the barrel presampler*, ATL-LARG-99-012, formula 3, p. 4.

[8] C. de La Taille, *New noise figures for the ATLAS EM calorimeter*, ATL-LARG-96-035, see also ATL-LARG-99-012, Annex 3.

[9] O. Martin, E. Monnier and S. Tisserant, *Update of some Geometrical Parameters for the ATLAS EM end-cap Calorimeter*, ATL-LARG-97-047, p. 4-5.

[10] Delphine Nicod, *EMTB User Guide*, version 0-2-19, see http://atlasinfo.cern.ch/Atlas/GROUPS/LIQARGON/TESTBEAM/emtbdoc.ps

[11] ANSYS Analysiz Guides version 5.5, 001083, 2nd edition, SAS IP inc.

[12] P. Pralavorio and D. Sauvage, *Review of the crosstalk in the module 0 of the Electromagnetic end-cap calorimeter*, ATL-COM-LARG-2001-004.

[13] ATLAS collaboration, *ATLAS Calorimeter Performance*, CERN/LHCC/96-40.

[14] P. Barrillon, F. Djama, L. Hinz, P. Pralavorio, *Uniformity scan in the outer wheel of electromagnetic end-cap calorimeter*, ATL-COM-LARG-2001-003.

[15] P. Perrodo, *Material between the presampler and the EMB module 0*, ATL-LARG-2001-002 (ATL-COM-LARG-2001-008).

Appendix 1. List of runs taken with the EM end-cap presampler.

Point 3							
Energy	+0.0 X_0	+0.91 X_0	+1.36 X_0	+1.82 X_0	+2.27 X_0	+2.73 X_0	+3.18 X_0
20 GeV	103687 103689			103726 103727		103709 103712	
40 GeV	103690 103691			103725 103728		103713 103738	
60 GeV	103692 103693			103724 193729		103715 103717	
80 GeV	103694 103695			103723 103730		103718 103735	
100 GeV	103696 103697			103722 103731		103719 103734	

Point 4’							
Energy	+0.0 X_0	+0.91 X_0	+1.36 X_0	+1.82 X_0	+2.27 X_0	+2.73 X_0	+3.18 X_0
20 GeV	103769			103827		103845	
40 GeV	103768	103857	103856	103826	103853	103846	103852
60 GeV	103767			103825		103847	
80 GeV	103766			103824		103848	
100 GeV	103765	103858	103855	103823	103854	103849	103851

Point 1’							
Energy	+0.0 X_0	+0.91 X_0	+1.36 X_0	+1.82 X_0	+2.27 X_0	+2.73 X_0	+3.18 X_0
40 GeV	103745			103748		103749	
100 GeV	103746			103747		103750	

Point 3’							
Energy	+0.0 X_0	+0.91 X_0	+1.36 X_0	+1.82 X_0	+2.27 X_0	+2.73 X_0	+3.18 X_0
40 GeV	103755			103756		103759	
100 GeV	103754			103757		103758	

Point 5’							
Energy	+0.0 X_0	+0.91 X_0	+1.36 X_0	+1.82 X_0	+2.27 X_0	+2.73 X_0	+3.18 X_0
40 GeV	103867	103866		103870	103876	103871	103874
100 GeV	103868	103865		103869	103877	103872	103873

The map of points is presented in figure 6.

Appendix 2. Beam energy, η, ϕ spread, cell noise used in simulation.

For the beam energy spread the following formula was used [5]:

$$\frac{dE}{E}(full\,width) = \Delta = \frac{\sqrt{k_1^2 + k_2^2}}{19.4}, \%$$

where the values of k_1, k_2 are given in the table below.

E_0	k_1, k_2	$\Delta, \%$
20 GeV	$\pm$5.	0.364
40 GeV	$\pm$4.	0.292
60 GeV	$\pm$4.	0.292
80 GeV	$\pm$2.	0.146
100 GeV	$\pm$2.	0.146
120 GeV	$\pm$2.	0.146

$E_{beam} = E_0 \cdot (1. + (rndm - 0.5) \cdot \Delta)$

E_{beam}	η_0	ϕ_0	σ_η	σ_ϕ
20 GeV	1.7119	0.5247	0.007	0.006
40 GeV	1.7113	0.5247	0.006	0.006
60 GeV	1.7170	0.5268	0.006	0.006
80 GeV	1.7147	0.5278	0.004	0.004
100 GeV	1.7140	0.5283	0.004	0.004

$$\eta_{beam} = \eta_0 + \sigma_\eta \cdot norm(0,1)$$
$$\phi_{beam} = \phi_0 + \sigma_\phi \cdot norm(0,1)$$

Noise added in one cell in simulation. Obtained from cluster noise in physics runs using selected random events.

presampler	strip	middle	back
2.50 MeV	20.5 MeV	54.0 MeV	38.0 MeV